Academic Journal of Science and Technology
ISSN: 2771-3032 | Vol. 11, No. 1, 2024

Thermal Cycling Stability of Ti-Zr-Nb-Al Shape Memory Alloy

Wentao Qu, Sizhu Huang

School of Mechanical Engineering, Xi'an Shiyou University, Xi'an, Shanxi 710065, China

Abstract: Shape memory alloys, as a novel class of intelligent materials, possess substantial application potential in the field of petroleum engineering at elevated temperatures. However, the complex downhole environment necessitates the alloy to endure alternating cycles of cold and heat, demanding both a high phase transformation temperature and excellent thermal cycling stability. This study focuses on a quaternary Ti-Zr-Nb-Al shape memory alloy, examining the thermal cycling stability of the Ti-20Zr-10Nb-xAl (x=1, 2, 3, 4 at%) alloys after subjecting them to 50 thermal cycles. Results indicate that the alloy composition, post 50 cycles, transitions from a single martensite α" -phase to a duplex microstructure comprising α"-phase and β-phase. Changes in Al content did not significantly affect the phase composition of the alloy in its thermally cycled state. As Al content increases, both the tensile strength and shape memory effect of the alloy initially improve before declining. In terms of shape memory properties, the Ti-20Zr-10Nb-2Al alloy sample exhibits the most favorable thermal cycling stability, characterized by a tensile strength of 692 MPa, an elongation of 6%, a shape memory effect of 0.96% under 4% pre-strain, a shape memory recovery rate of 38%, and a Vickers microhardness of 381 HV.

Keywords: Ti-Zr-Nb-Al; Microstructure; Mechanical properties; Shape memory effect; Thermal cycling stability.

1. Research Background

Shape memory alloys (SMAs) are widely utilized across various domains such as aerospace, mechanics, electronics, and medicine due to their distinctive shape memory effect and superelasticity[1]. Metal intelligent actuators fabricated from SMAs can replace traditional mechanical equipment with complex structures, enhancing system reliability and automation levels. They hold significant potential for application in the aviation and petroleum industries under high-temperature environments[2]. For instance, using SMAs to manufacture sealing components in oil well packers instead of traditional rubber seals can simplify the product design, extend service life, and substantially reduce the cost of oil production[3].

However, for the widespread application of SMAs in the petroleum industry, they must possess higher transformation temperatures and more stable performance. Due to the limitations of the intrinsic properties of Ni-Ti shape memory alloys, their transformation temperatures typically fall below 373 K, making them unsuitable for use in high-temperature environments[4]. Thus, developing new high-temperature shape memory alloys with good comprehensive performance has remained an important research direction in this field. Long-standing research on high-temperature shape memory alloys has primarily centered on Ni-Ti-X, Ti-X-Ni, Ni-Al based, Cu-based, and Ni-Mn-Ga alloy systems[5-6]. Although these alloys can achieve high transformation temperatures (373–873K) through compositional adjustments, they all exhibit varying degrees of drawbacks that hinder their practical implementation.

The new titanium-based high temperature shape memory alloy shows the characteristics of higher transformation temperature, rendering them more suitable for application in high-temperature subsurface environments[7]. Nonetheless, the intricate nature of subsurface conditions, characterized by cyclic thermal variations, imposes stringent requirements on the inherent thermal cycling stability of the alloys. Consequently, examining the alterations in microstructure, phase transformation, and functional properties of shape memory alloys under standard conditions as well as subsequent to multiple thermal cycles, and ascertaining whether their multifaceted performance aligns with engineering specifications, holds not only considerable scientific significance but also profound practical implications.

Therefore, this study elects to introduce trace amounts of Al into the Ti-20Zr-10Nb alloy composition, with the intent of augmenting its mechanical properties while maintaining a higher transformation temperature[8]. Building upon this, the investigation delves into elucidating the patterns through which thermal cycling influences the microstructure, phase transformation characteristics, mechanical properties, and shape memory effects of the Ti-Zr-Nb-Al shape memory alloy. The objective is to assess the thermal cycling stability of the Ti-Zr-Nb-Al alloy, thereby providing theoretical substantiation for the practical application of Ti-Zr-Nb-Al high-temperature shape memory alloys.

2. Experimental

For the experimental requirements, Ti-20Zr-10Nb-xAl (x=1, 2, 3, 4 at%) alloys were prepared by vacuum arc melting high-purity titanium (99.9%), zirconium (99.9%), niobium (99.9%) and aluminum (99.9%) in a water-cooled copper crucible in an ultra-pure Ar atmosphere. Ingots weighing approximately 150 g were turned over and re-melted five times to ensure compositional homogeneity. The ingots were sealed under vacuum in quartz tubes and homogenized at 1173 K for 2 h followed by water quenching. Then, the samples were hot-forged at 1123 K into 5-mm-thick plates and cold-rolled until the thickness was reduced by 80%. These specimens were rolled down to a thickness of 1 mm and finally cut into several 10 mm × 10 mm × 1 mm rectangular samples and tensile samples as per the specifications illustrated in Figure 1. The surfaces were cleaned via mechanical grinding to remove contaminants,

after which the rolled plates were sealed into quartz tubes under a vacuum of at least 0.25 Pa. The plates were then annealed at 873 K for 0.5 h and water quenched by breaking the quartz tube. The plates were cut parallel to the rolling direction into the shapes appropriate for each test using a wire cut electrical discharge machine.

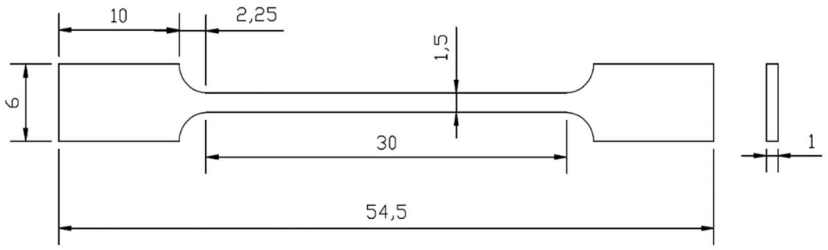

Figure 1. Tensile test sample specifications

Subsequently, the alloy samples underwent thermal cycling treatment, the specifics of which were as follows: The samples were subjected to thermocycling using a resistance furnace with a temperature cycle set between 300 to 700 K, with a heating and cooling rate of 10 K/min, performing 50 cycles for each sample.

The microstructure of the alloy samples was observed using an Axiovert405M optical microscope (OM), with test samples being 10 mm × 10 mm × 1 mm rectangular pieces. The samples were etched in a solution of HF: HNO3: H2O = 1: 4: 5 for 30 to 60 seconds before examination.

Phase analysis of the alloy samples was conducted using an XRD-6000 X-ray diffraction instrument (XRD), with test samples being 10 mm × 10 mm × 1 mm rectangular pieces polished to 2000 grit. The scanning speed of the XRD was set at 5°/min, with a scanning range from 20° to 90°, and operating voltage and current at 40 kV and 200 mA.

The phase transition characteristics of the alloy were tested using a DSC204 differential scanning calorimeter. Before the experiment, alloy samples weighing approximately 10 mg were cut using a cutting machine. The heating and cooling rates for the DSC experiment were set at 12°C/min, with the temperature range set from 300 K to 700 K.

Tensile testing was performed on the alloy samples using a CMT5105D universal testing machine, with a gauge length of 25 mm and a tensile rate of 0.5 mm/min. The strain associated with the shape memory recovery strain (ε_{SME}) and the shape memory recovery ratio (η) were calculated using the following formulas:

$$\varepsilon_{SME} = \frac{L_1 - L_2}{L_0} \times 100\% \quad (1)$$

$$\eta = \frac{L_1 - L_2}{L_1 - L_0} \times 100\% \quad (2)$$

In this formula, three types of length are defined as follows: (1) initial length of alloy sample L_0, (2) The length of the alloy sample after tensile unloading L_1, (3) The length of the alloy sample after heating L_2.

3. Results and Discussion

3.1. Microstructures of alloy after thermal cycling

Fig.2 shows the X-ray diffraction (XRD) patterns of the Ti-20Zr-10Nb-xAl (x=1, 2, 3, 4 at%) alloy after 50 times thermal cycling treatments. After 50 times thermal cycling treatments, all compositions of the Ti-20Zr-10Nb-xAl (x=1, 2, 3, 4 at%) alloy exhibit a dual-phase microstructure consisting of a body-centered cubic β-phase and an orthorhombic martensitic α″-phase. When the Al content increased from 1% to 4%, no significant changes are noted in the XRD profiles. The primary characteristic peaks appear at 38.66°, 55.48°, 64.56°, and 69.72°, corresponding to crystallographic planes of β (110), β (200), α″ (130), and β (211).

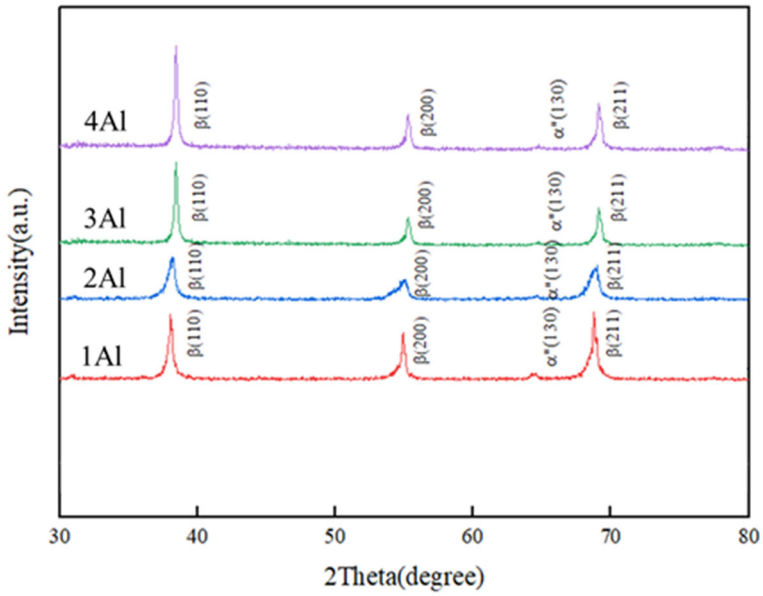

Figure 2. XRD pattern of Ti-20Zr-10Nb-xAl (x=1,2,3,4 at.%) alloy after 50 times thermal cycling treatments

Prior to thermocycling, the Ti-20Zr-10Nb-xAl (x=1, 2, 3, 4 at%) alloy samples were composed solely of the martensitic α″-phase. However, after multiple thermocycles, a substantial amount of the martensitic α″-phase transformed into the β-phase. Due to the relatively slow cooling rate during the thermocycling process, only a minor fraction of the high-temperature austenite β-phase underwent martensitic transformation intoα″-phase, resulting in the retention of a significant amount of the β phase within the alloy. Consequently, the alloy exhibited a duplex microstructure consisting of α" martensite and β phases after multiple thermocycles. As the number of thermocycles increased, the phase composition of the alloy ceased to change. Therefore, despite varying Al contents in the Ti-20Zr-10Nb-xAl (x=1, 2, 3, 4 at%) alloy samples, the phase composition remained consistent following thermocycling experiments.

The phase composition of the Ti-20Zr-10Nb-xAl alloy is directly related to the heat treatment process. Rapid cooling promotes the formation of the martensitic α"-phase, whereas slower cooling rates result in a significant amount of the austenitic β phase failing to transform timely into the α" martensite, such that a substantial amount of the β phase remains in the microstructure when the alloy reaches room temperature. Since α" martensite is a metastable phase, it cannot remain stable during thermal cycling. With increasing temperature, a considerable amount of the α" martensite transforms into the high-temperature β phase. Conversely, during cooling, only a small portion of the β phase austenite converts back to α" martensite. Consequently, the β-phase accumulates gradually throughout the thermal cycling until a phase equilibrium is reached. According to XRD patterns, the Ti-20Zr-10Nb-xAl alloy maintains a duplex microstructure consisting of α" and β phases even with continuous thermal cycling.

Fig.3 shows the metallographic microstructures of the Ti-20Zr-10Nb-xAl (x=1, 2, 3, 4 at%) alloys after 50 thermocycles. As shown in Fig.3a, the Ti-20Zr-10Nb-1Al alloy exhibits a very fine equiaxed grain structure after thermocycling, with grain sizes ranging from 2 to 3 μm. This is slightly smaller than the grains observed in the alloy prior to thermocycling. Fig.3b, Fig.3c, and Fig.3d reveal that the Ti-20Zr-10Nb-2Al, Ti-20Zr-10Nb-3Al, and Ti-20Zr-10Nb-4Al alloys all contain black, particulate α" martensite with grain sizes varying from 2 to 4 μm. This is not markedly different from the microstructure observed in the alloys before thermocycling.

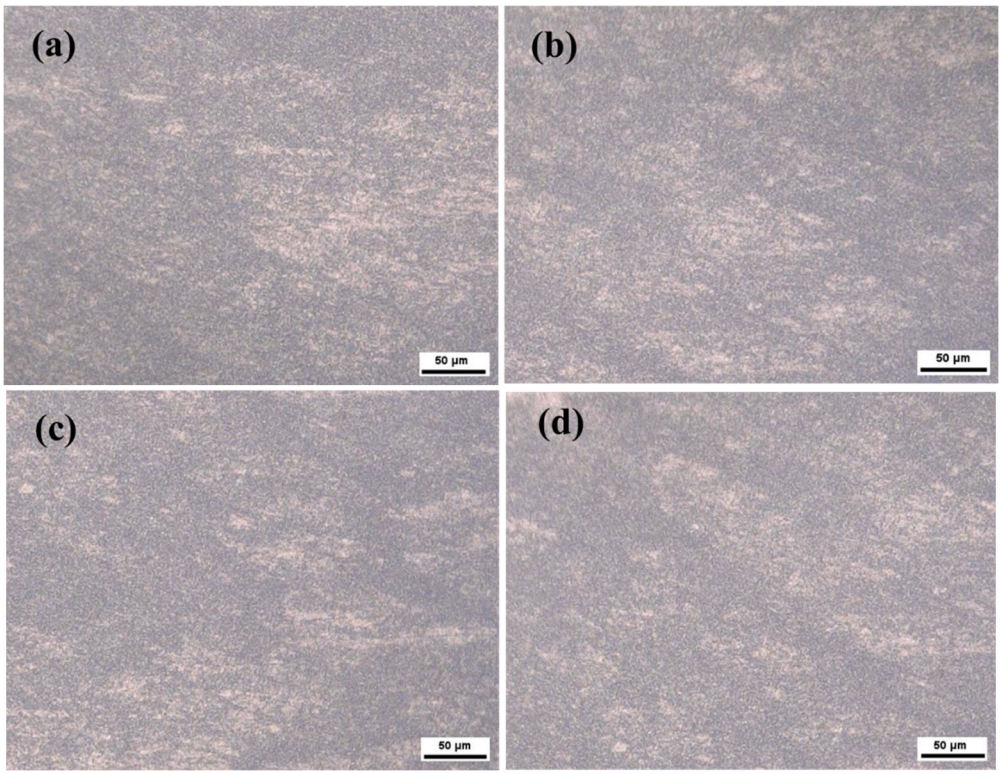

Figure 3. Metallographic organization of Ti-20Zr-10Nb-xAl alloy after 50 times thermal cycling treatments: (a) 1at%, (b) 2at%, (c) 3at%, (d) 4at%

3.2. Phase transformations of alloy after thermal cycling

After 50 times thermal cycling treatments, the differential scanning calorimetry (DSC) curves of the Ti-20Zr-10Nb-xAl (x=1, 2, 3, 4 at%) alloys are shown in Fig.4. Similar to the phase transformation characteristics before thermocycling, no exothermic peaks are observed in the cooling curves of the Ti-20Zr-10Nb-xAl (x=1, 2, 3, 4 at%) alloys. Therefore, this section focuses solely on the phase transformation behavior during the heating process of the alloy samples. After 50 times thermal cycling treatments, the reverse martensitic transformation characteristic temperatures of the Ti-20Zr-10Nb-1Al alloy are determined to be: A_S =530K, A_f=566K, A_p =542K. For the Ti-20Zr-10Nb-2Al alloy, the reverse martensitic transformation characteristic temperatures are: A_S=508K, A_f=534K, A_p=521K. In the case of the Ti-20Zr-10Nb-3Al alloy, the characteristic temperatures are: A_S =492K, A_f =522K, A_p =506K. Lastly, for the Ti-20Zr-10Nb-4Al alloy sample, the characteristic temperatures are: A_S=480K, A_f=514K, A_p=494K.

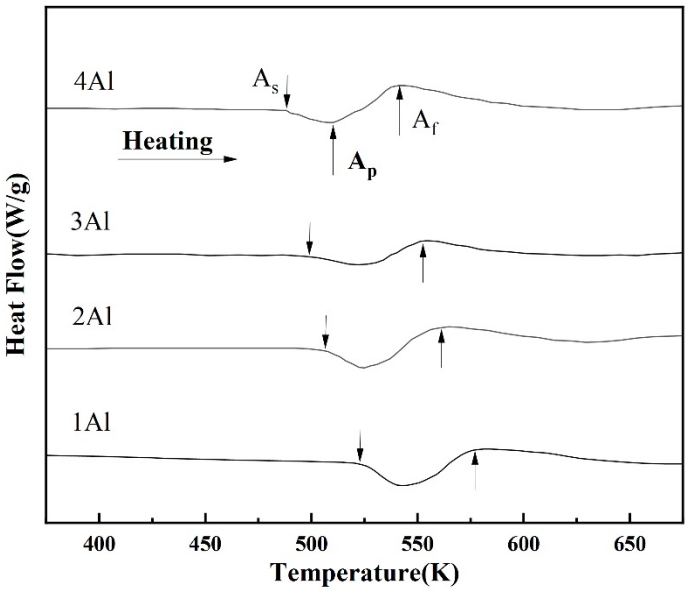

Figure 4. DSC curves of Ti-20Zr-10Nb-xAl (x=1,2,3,4 at.%) alloy after 50 times thermal cycling treatments

After 50 times thermal cycling treatments, the Ti-20Zr-10Nb-xAl (x=1, 2, 3, 4 at%) alloys, irrespective of their compositional variations, exhibited a generally consistent trend in the alteration of their characteristic phase transformation temperatures. Specifically, the phase transformation temperatures of these alloys decreased by approximately 10K and subsequently remained largely stable. Even with the continuous increase in the number of thermal cycles, there was minimal further change in the phase transformation temperatures of the alloys. It can be inferred that the impact of thermal cycling on the phase transformation characteristics of the Ti-20Zr-10Nb-xAl alloys, across their various compositions, is relatively minor. The result suggests that the characteristic phase transformation temperatures of the Ti-20Zr-10Nb-xAl (x=1, 2, 3, 4 at%) alloys are inherently stable, and their phase transformation properties are theoretically capable of satisfying the temperature cyclic requirements of high-temperature subsurface environments.

3.3. Mechanical properties

After 50 times thermal cycling treatments, the stress-strain curves of the Ti-20Zr-10Nb-xAl (x=1, 2, 3, 4 at%) alloys are depicted in Fig.5. Results from tensile testing indicate that the tensile strength of the Ti-20Zr-10Nb-1Al alloy post-50 thermal cycles is 685 MPa with an elongation of 6%. Compared to its pre-cycled state, there is a slight reduction in tensile strength and a significant decrease in elongation. The Ti-20Zr-10Nb-2Al alloy demonstrates a tensile strength of 692 MPa and an elongation of 6% after 50 cycles, both of which have decreased compared to the uncycled condition. The Ti-20Zr-10Nb-3Al alloy exhibits a tensile strength of 760 MPa and an elongation of 9%, showing a slight reduction in strength post-cycling, while the elongation is notably higher than that of other alloys. Finally, the Ti-20Zr-10Nb-4Al alloy maintains a tensile strength of 775 MPa with an elongation of 5% after 50 cycles; its tensile strength is essentially unchanged, but there is a significant reduction in elongation compared to its pre-cycled state.

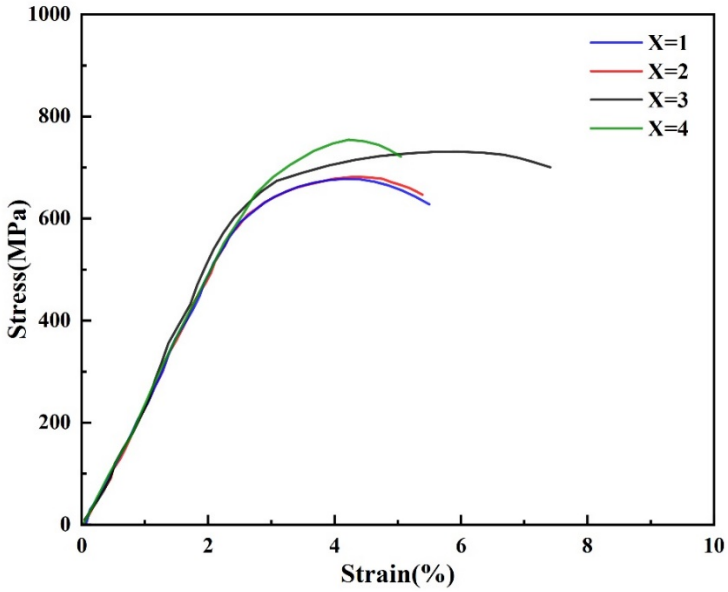

Figure 5. The stress-strain curves of Ti-20Zr-10Nb-xAl (x=1,2,3,4 at.%) alloy after 50 times thermal cycling treatments

The results observed are attributed to the fact that the alloy samples, prior to thermal cycling, were in a metastable martensitic α"-phase. During the tensile process, a martensitic phase transformation occurred. Subsequent to thermal cycling, the grains transformed into finer β-phase grains, with an increased grain boundary area. This larger grain boundary area impedes the movement of dislocations, thereby enhancing the material's strength and hardness. However, the presence of β-phase grains also led to an increase in the sample's brittleness, resulting in a reduction in the alloy's elongation. As the number of thermal cycles increases, the martensitic α"-phase becomes more predominant, causing a slight decrease in the tensile strength of the alloy samples.

3.4. Shape memory effect

After 50 times thermal cycling treatments, the shape memory effect (SME) of the Ti-20Zr-10Nb-xAl (x=1, 2, 3, 4 at%) alloys under different pre-strains were measured through tensile tests. The shape memory recovery strain (ε_{SME}) and the shape memory recovery ratio (η) were calculated from the experimental data and plotted in Fig.6 and Fig.7. The figures illustrate that the Ti-20Zr-10Nb-2Al alloy exhibits the highest shape memory recovery strain and recovery rate among all compositions after 50 times thermal cycling treatments. This indicates that the Ti-20Zr-10Nb-xAl alloy with an aluminum content of 2 at% demonstrates superior thermal cycling stability in terms of shape memory properties.

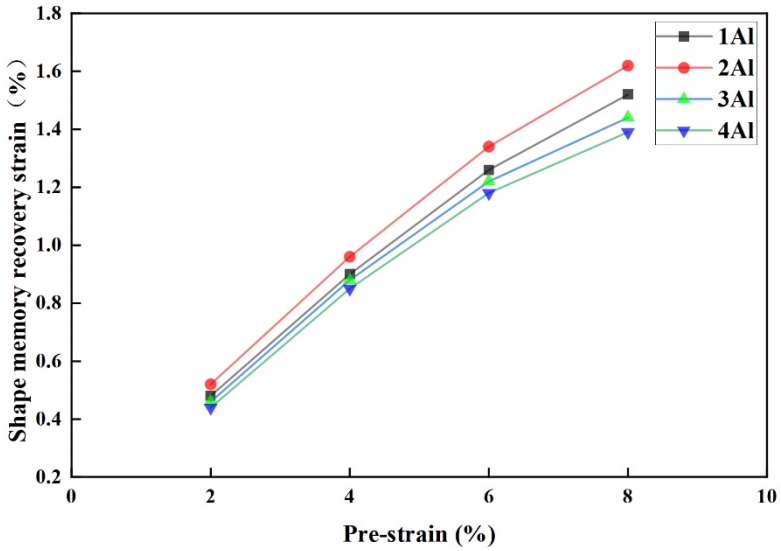

Figure 6. The shape memory recovery strain of Ti-20Zr-10Nb-xAl (x=1,2,3,4 at.%) alloy after 50 times thermal cycling treatments

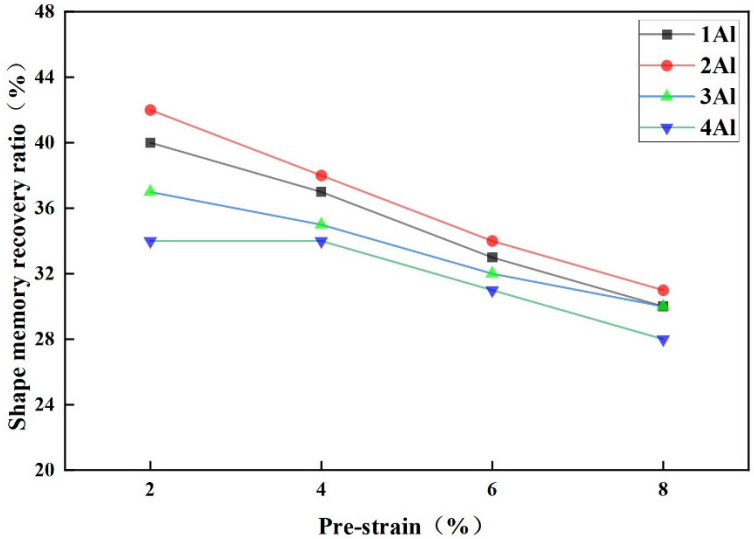

Figure 7. The shape memory recovery ratio of Ti-20Zr-10Nb-xAl (x=1,2,3,4 at.%) alloy after 50 times thermal cycling treatments

The experimental outcomes can be attributed to the fact that upon thermocycling treatment, a significant quantity of the martensitic α"-phase in the Ti-20Zr-10Nb-xAl alloy transforms into the austenitic β-phase. However, once the amount of the β-phase reaches a certain threshold, it hinders the continuation of the reverse martensitic transformation, making the transformation of α"-phase into β-phase increasingly difficult. This leads to the dynamic equilibrium between α"-phase and β-phase, where their quantities remain relatively constant. Consequently, after a certain number of

thermocycles, the Ti-20Zr-10Nb-xAl alloy retains a substantial amount of α" martensite, allowing the alloy's shape memory properties to remain essentially stable.

4. Conclusion

(1) After undergoing 50 times thermal cycling treatments, the Ti-20Zr-10Nb-xAl (x=1, 2, 3, 4 at%) alloys transformed from a single metastable martensitic α"-phase to a dual-phase microstructure consisting of β-phase and α"-phase, with little effect of Al content on the alloy's phase composition. The microstructure did not exhibit significant changes and remained as equiaxed grains.

(2) The Al content had a minimal influence on the phase transition temperatures of the heat-cycled Ti-20Zr-10Nb-xAl alloys. The phase transformation temperatures of alloys with different compositions exhibited a similar trend, where the transformation temperatures decreased by approximately 10K after an increase in the number of thermal cycles and then remained largely unchanged.

(3) After 50 times thermal cycling treatments, the tensile strength of the Ti-20Zr-10Nb-3Al alloy was maintained at 760 MPa, with an elongation of 9%, the highest among the four alloy compositions, indicating superior thermal cycling stability in terms of mechanical performance. Additionally, the Ti-20Zr-10Nb-2Al alloy demonstrated the highest shape memory recovery strain and recovery rate, suggesting the best thermal cycling stability in terms of shape memory properties.

References

[1] Churakova, Gunderov. Microstructural and Mechanical Stability of a Ti-50.8 at.% Ni Shape Memory Alloy Achieved by Thermal Cycling with a Large Number of Cycles[J]. Metals, 2020, 10(2).

[2] Pérez Sierra A.M., Pons J., Santamarta R., Karaman I. Stability of a Ni-rich Ni-Ti-Zr high temperature shape memory alloy upon low temperature aging and thermal cycling[J]. Scripta Materialia, 2016, 124.

[3] Sun B., Meng X. L., Gao Z. Y., Cai W. Stability of Phase Transformation Temperatures During Cycling of Ti-15.8Nb-4.94Al-0.06Sc Shape Memory Alloy[J]. Journal of Materials Engineering and Performance, 2018, 27(12).

[4] Zhang Yanqing, Jiang Hengxing, Liu Xingjun, et al. Thermal cycle stability of Co64V15Si17Al4 high-temperature shape memory alloy[J]. Materials Letters, 2020, 260.

[5] Wang Jun, Li Qiquan, Xiong Chengyang, Li Yan, Sun Baohui. Effect of Zr on the martensitic transformation and the shape memory effect in Ti-Zr-Nb-Ta high-temperature shape memory alloys[J]. Journal of Alloys and Compounds, 2018, 737.

[6] Li Qiquan, Ma Xiaolong, Xiong Chengyang, Qu Wentao, Li Yan. Effects of annealing temperature on microstructures and shape memory effect of Ti-19Zr-11Nb-2Ta alloy sheets[J]. Journal of Alloys and Compounds, 2022, 897.

[7] Liu Jikui, Zhang Xiangyun, Yuan Zizhou, Structures and properties of biocompatible Ti-Zr-Nb-Fe-Mo medium entropy alloys[J]. Materials Today Communications, 2022, 32.

[8] Yu Z G, Xiong C Y, Xue P F, et al. Shape memory behavior of Ti–20Zr–10Nb–5Al alloy subjected to annealing treatment[J]. Rare Metals, 2016, 35(11): 831-835.